10th September 2005: a bolide airblast in the Gulf of Naples (Southern Italy).

L. D'Auria, E. Marotta, M. Martini, P. Ricciolino
Istituto Nazionale di Geofisica e Vulcanologia - Osservatorio Vesuviano

March 13, 2006

Abstract

On 10th September 2005 at 17:11 local time (15:11 GMT) a loud boom was heard on the Ischia island. A clear seismic signal was also recorded by the seismic monitoring network of the Neapolitan volcanic areas (Ischia, Campi Flegrei and Mt. Vesuvius) and on a regional station (Mt. Massico). On the base of the seismic recordings and on acoustic phenomena reports, we relate this event to the airblast of a bolide at about 15 Km SW of Ischia at an elevation of about 11.5 Km. The location has been obtained through probabilistic non-linear traveltime inversion in a realistic atmospheric model including wind effect. We will show, using statistical estimators, how the traveltime pattern is due to both atmospheric winds and bolide trajectory. Using the same reasoning we discard a human origin (supersonic jet or sea-air missile). In addition, we propose also a new algorithm for a fast acoustic traveltime computation for a moving source.

1 Introduction

Large bolides, entering in the atmosphere at hypersonic velocities, are always accompained by powerful shock waves ([19]). When these waves reaches the ground, they are often perceived as a loud boom by peoples and are sometimes recorded by seismic ([9], [12] and [18]) and infrasonic networks ([4] and [6]).

The atmospheric path of bolides depends on their entrance velocity (that usually ranges from 7.8 to 70.8 Km/s) ([15]), on the entrance angle (0^o for grazing bolides) and on the physical properties of the meteoroid (mass and composition). During the first seconds of the path the bolide impacts the rarified gases of the upper atmosphere, starting its deceleration. Because of the high velocity, the effect of the gravity on the path is negligible, leading to an almost linear trajectory ([24]). When the bolide encounters the progressively denser gases of the lower atmosphere, it begins to suffer of strong shear stresses. This may led to a sudden fragmentation and blasting of the meteoroid ([7]). During the first phase a Mach cone radiates from the almost linear trajectory. Then, after the airblast, a quasi-spherical wavefront radiates from the blasting point.

In this paper we examine different models that may be able to justify observed acoustic effects, traveltimes and waveforms. The simplest model consists

in a point source in the atmosphere. At a first sight, we believed that the phenomenon of 10th Sep. 2005 was related to a geothermal explosion, since similar phenomena (altough with significantly minor acoustic and seismic effects) occurred in the past on the Ischia island. Trials of locating the source on the ground and to model observed sound amplitudes failed. Then we tried to locate the source as an atmospheric explosion using a simple point source model. The result (see section 4) suggested, that the hypothesis was plausible, but we first tried to exclude an artificial origin. The observation of clear "N-waves" ([10]) at station SOB (Fig. 1 and Fig. 5) lead us to the conclusion that the phenomenon was caused by a supersonic or hypersonic object. We tried then to justify observed traveltimes with a model of a supersonic jet following a linear path (see section 6). Results indicated a poor fit of the traveltimes and a significant disagreement with observed acoustic effects. The same conclusion is reached when considering the model of a sea-air missile, starting from the sea level, travelling at supersonic velocity and exploding in the atmosphere (section 7).

At this point we considered the hypothesis that the phenomenon was generated by a bolide entering in the atmosphere at hypersonic velocity (8). Unluckily this hypothesis is not supported from any direct visual observation, probably because of the daylight and of a cloudy sky, so we based all our analysis on seismic data (section 3) and on acoustic reports of the "boom" (section 2).

Following existing literature ([10], [12], [18]), we first considered a simple model of a bolide entering in the atmosphere with a constant velocity. The result seems to be consistent with both traveltimes and acoustic phenomena. However, waveforms observed in Ischia do not seems to follow the "N-wave" model, but they are more likely related to an explosion. Then we hypotized that part of the network recorded (as "N-wave") the shock wave coming from the bolide trajectory, while another part recorded mainly the pressure wave generated by the terminal airblast of the bolide. This model gives the best fit for traveltimes and justifies both the observation of "N-waves" on part of the network and of different waveforms at Ischia (section 9). Using this model we may compute precisely the bolide trajectory and make some inference about its entering velocity in the atmosphere (section 11).

Concerning the traveltime modeling, most of the techniques presented in recent papers, require only simple propagation model, as constant speed ([12], [18]), linearly varying speed and linearly varying temperature ([24]). For this simple models analytical solution may be obtained. Realistic atmospheric models requires more complex modeling techniques as ray-tracing ([8]). In this paper we use a fast technique, the Podvin-Lecomte algorithm ([16]) widely used in Seismology. The detailed implementation of the technique for moving sources is illustrated in Appendix A.

The search for a best fit model that justifies observed traveltime is a non-linear problem. The most common approach for solving this kind of problem consists in starting from a reference model and, iteratively, moving toward the best fit model through successive perturbations ([20])([18]). Anyway this technique may lead to erroneous solutions in case of strongly non-linear problems ([21]). An alternative but time consuming approach is to perform a full grid search over the whole range of model parameters ([10], [12]). In this work we develop a hybrid non-linear technique that performs a smart exploration of the model space, avoiding regions with a high misfit and, at the same time, ensuring a full exploration of local minima. The approach consists in a mixing of

a global exploration, using a nested grid search (see Appendix B), and a local optimization, using the Downhill Simplex method of [14].

In the final part the choice among all the models is performed on the basis of the Akaike Information Criterion (AIC) ([1]). This statistical criterion allows to select among models having a different number of parameters and a different final misfit. In this way we are confident to choose the best model, without performing an "overfit" of data noise.

2 Acoustic effects

Six days after the 10th Sep. 2005 event, an interview to about 60 peoples living in Ischia was performed. Detailed informations about the intensity and the nature of the "boom" were asked to the people. After a careful review of collected informations we classify the degree of perception into three categories. The "red" one groups all the answers that indicated a certain degree of scare and concern about the phenomenon. The "yellow" group collects all the answers where the "boom" has been clearly heard, but with an intensity that caused no more than curiosity about it. At last, the "green" class, groups the answers where the sound has been barely or not heard.

Interview points, classified as "red", "yellow" or "green" have been precisely located on a map and areas with common class have been contoured with the corresponding colour (Fig. 2). On the basis of the interviews and on the observed intensity pattern we can draw some conclusions.

All the interviewed people claimed that the phenomenon was not accompained by ground shaking.

Some people reported the shaking of windows and the phenomenon has been felt also by some deaf people. For this reason we deduce that the "boom" was accompanied by a huge infrasonic pressure transient.

At least six people perceived the sound as coming from south (although with some difference) (Fig. 2) and some people report that the sound resembled the "boom" of a supersonic jet, believing that the sound was coming from above.

Finally, looking at the map with observed acoustic intensities, it is clear that the sound source is not located on or very close to the island, because the "red" region spans the whole area.

It is important to notice that no "boom" or similar phenomena has been reported outside Ischia island.

3 Waveforms and traveltimes

The seismic monitoring network managed by the "Osservatorio Vesuviano", section of Istituto Nazionale di Geofisica e Vulcanologia (INGV-OV) is designed to monitor local seismicity in the volcanic areas of Vesuvius, Campi Flegrei and Ischia. This network is complemented with other 6 regional stations (as MSC), deployed within the radius of 70 Km from volcanic areas and with the whole italian seismic network managed by Centro Nazionale Terremoti (INGV-CNT). Most of the stations are equipped with short-period sensors (11 3C and 21 1C), while three seismic stations are equipped with broadband sensors. In Fig. 1 the map of the seismic network is shown.

The signal has been recorded by all the stations in Ischia and Campi Flegrei. In the Vesuvius area the signal has been well recorded by the summit stations, far away from urbanized areas. Stations situated at lower elevations, near the ring of towns around Mt.Vesuvius (as Herculaneum HR9 and Pompei PPV) did not record a clear signal because of the high level of cultural noise. An interesting observation is the absence of evident signals at the 3C station SOR situated at the western tip of the Sorrento Peninsula. This station usually shows an excellent signal/noise ratio, but lays on a solid limestone, whereas most the other stations lays on poorly consolidated pyroclastic rocks.

The pressure wave generated by supersonic object moving in the atmosphere have a typical shape, resembling a "N" letter, for this reason they are often indicated as "N-waves" (Fig. 6A). The theoretical vertical ground motion induced by "N-wave" pressure variations should be roughly equal to the opposite of the pressure pattern ([22]) (Fig. 6B). Since our seismograms represents the velocity of the ground motion that is the derivative of the ground displacement, then the theoretical velocity seismogram should resemble a "W" shaped waveform (Fig. 6C). In practice, due to the non-flat spectral response of the ground and to the instrumental response function, the real seismogram (Fig. 6D and Fig. 6E) will be quite different. After these pressure forced movements the shallow layers may continue resonating, giving an oscillatory signature to waveforms. This is specially true on poorly consolidated soils of alluvial ([12]) or pyroclastic origin, where the spectral response of the soil strongly affects waveforms.

In Fig. 3 and Fig. 4 the recorded waveforms are shown. They are aligned to the picked supposed sonic wave arrival. Some of the stations (e.g. BKE) show a small amplitude signal, preceeding the strong acoustic arrival. This may be interpreted as a ground roll (composed mostly of Rayleigh waves) that travels faster than the infrasonic signal. Traveltimes for each station are listed in Tab. 12. They are complemented with an uncertainty value that depends on the signal/noise ratio and on the presence of a precursory ground roll that may affect negatively the correct phase picking.

Unfortunately, at the time of the event the timing systems of the broadband and the short period stations were different, with a systematic bias between them. For this reason we do not include the arrival time of the broadband station SOB in the inversions, but we show the waveform of its vertical component in Fig. 5. The velocity seismograms show the typical "W" shape, while their integral shows a reverse "N" shape. These shapes are usually related to the impact on the ground of shock-wave related pressure disturbance ([11], [12]). It is remarkable the similarity of the velocity seismogram at SOB (Fig. 5) with the theoretical response of a broadband sensor to an "N-wave" (Fig. 6D and the similarity between waveforms of some short period recording (e.g. POZ) (Fig. 4) and the theoretical seismogram in Fig. 6E.

4 An atmospheric explosion?

After unsuccessfull trials of locating the sound source on the ground, we tried to locate it into the atmosphere. The inverse problem for locating an atmospheric point source is very similar to a common earthquake location problem. We solve the inverse problem in a probabilistic fashion ([23]). The model parameter vector for this problem is $\mathbf{m} = (t_0, x_0, y_0, z_0)$, where t_0 is the origin time of the

event and x_0, y_0, z_0 are the source coordinates in a cartesian reference system (see Fig. 1). The theoretical traveltime may be written as:

$$t_i^{theo} = t_0 + t_i^{prop}, \tag{1}$$

where i is the receiver index and $t_i^{prop} = t_i^{prop}(x_0, y_0, z_0)$ is the propagation time from the source to the i-th receiver or viceversa. This time may be obtained using the Podvin and Lecomte algorithm ([16]), (see Appendix A for details).

Because of the nature of the previous equation, it is easy to show that the parameter t_0 can be discarded from the inverse problem and its maximum likelihood estimate can be retrieved directly from the remaining parameters using the formula:

$$t_0 = \frac{\sum_i \frac{\left(t_i^{obs} - t_i^{prop}\right)}{\sigma_i^2}}{\sum_i \frac{1}{\sigma_i^2}}, \tag{2}$$

where t_i^{obs} is the i-th observed arrival time.

Once traveltimes have been computed, the unnormalized "a posteriori" probability density function (p.d.f.) may be defined as ([23]):

$$\rho(\mathbf{x}) = e^{-E(\mathbf{x})}, \tag{3}$$

where $E(\mathbf{x})$, the error (or misfit) function, is defined as:

$$E(\mathbf{x}) = \sum_i \frac{\left(t_i^{obs} - t_i^{calc}\right)^2}{\sigma_i^2}. \tag{4}$$

In the previous expression the squared residuals for each observed traveltime are weighted using the picking uncertainty σ_i.

The velocity model for the whole atmosphere has been obtained using two different models. The lower part (0 to 25 Km) comes from the NOAA-CIRES CDC (NCEP/NCAR Reanalysis 1) database ([2]). Temperature values for the considered area, at the event time (15:10 GMT), have been obtained by linear interpolation both in space and time. Available spatial points used for spatial interpolation are shown in Fig. 1 as red points, while available times used for interpolation are 12:00 and 18:00 GMT (Fig. 7). The upper part, instead, comes from the US Standard 1976 atmosphere model ([3]). The sound speed is then obtained through the relation ([8]):

$$c = \sqrt{\gamma_g R T} = \sqrt{402.8\, T}, \tag{5}$$

where $\gamma_g = c_p/c_v$ is the ratio between isobaric and isovolumetric specific heats of the air, R is the gas constant ($272\, Jkg^{-1}K^{-1}$) and T is the temperature (in K).

The final location (Model 1A in Tab. 12) shows a source located about $20\, Km$ SW of Ischia at an height of about $22\, Km$. Statistical estimators gives an uncertainty on the source location less than $500\, m$. The range of parameters explored is showed in Tab. 12 and the final misfit in Tab. 12. The traveltime fit with observed data (Fig. 8) is poor, showing large residuals. Furthermore we observe a systematic pattern of negative residuals on the Vesuvius area. This suggest that probably a traveltime perturbation by atmospheric winds occurrs.

5 Wind effect on traveltimes

To analyze the effect of the wind on traveltimes different approaches may be used ([8]). We suppose that the average wind velocity is small compared with sound speed and that the wind shear effect is negligible. Under these conditions, an acoustic signal propagates with an effective speed ([8]):

$$c_{eff} = \overline{c_{sound}} + \overline{\mathbf{u}} \cdot \widehat{\mathbf{r}}, \tag{6}$$

where $\overline{c_{sound}}$ is the average sound speed along the path, $\overline{\mathbf{u}}$ is the average wind velocity and $\widehat{\mathbf{r}}$ is a unitary vector from the source to the receiver. Eq.6 just says that the effective sound speed is increased in the direction of the prevailing winds and decreased in the opposite one. The propagation time is then:

$$t_i^{wind} = d\, c_{eff}^{-1}, \tag{7}$$

where d is the distance between the source and the receiver. Substituting eq.6 in eq.7, expanding the left side to the first order we obtain:

$$t_i^{wind} \simeq d\, c_{sound}^{-1} \left(1 - \frac{\overline{\mathbf{u}} \cdot \widehat{\mathbf{r}}}{\overline{c_{sound}}}\right). \tag{8}$$

The previous expression clearly indicates that the wind effect acts as a small perturbation on the traveltime in windless conditions $t^{nowind} = d\, c_{sound}^{-1}$.

In the same way followed for obtaining the atmospheric temperature, we retrieved a wind speed model for the range 0-25 Km using the NOAA-CIRES CDC (NCEP/NCAR Reanalysis 1) database ([2]) and interpolating data as for air temperature (see previous paragraph). Wind speed values used in this paper are shown in Fig. 9. The wind speed is assumed to be zero above 25 Km.

The location of a point source including the wind effect is shown in Tab. 12 (Model 1B). A significant drop of the final model misfit is achieved (Tab. 12) indicating that the wind effect is far from being negligible in modeling and locating atmospheric explosions. The theoretical traveltimes with their residuals are shown in Fig. 10, while Fig. 11 shows the traveltime difference between the wind and the windless case. The magnitude of the perturbation ($10^{-1} \div 10^{0} s$) is clearly not negligible, being of the same order of the final residuals.

6 Was the boom caused by a supersonic jet?

The clear observation of "N-waves" at SOB (Fig. 5) implies that, at least at some stations, the signal is related to a shock-wave generated by a supersonic or hypersonic object. For this reason we tested the hypotesis that the observed phenomenon was related to a supersonic jet traveling at low altitude. We suppose a linear trajectory at constant velocity, so the parameter vector for this hypothesis is $\mathbf{m} = (x_0, z_0, v, \theta, \gamma)$, where (x_0, z_0) is the intersection point of the jet trajectory with the plane $y = 0$, v is the jet velocity, θ is the angle formed by the trajectory with the horizontal plane and γ is the azimuth.

The forward traveltime modeling for a supersonic object is performed using the algorithm illustrated in Appendix A. The inverse problem in the case of a moving source is no more trivial as for the point source location, since the

parameters describing the model are related to observed data in a highly non-linear way. To overcome at least partially this difficulty, we perform a global search on parameters (x_0, z_0), defining a misfit function:

$$E^{out}(x_0, z_0) = E\left(x_0, z_0, v^b, \theta^b, \gamma^b\right), \tag{9}$$

where $\left(v^b, \theta^b, \gamma^b\right)$ are the best fit parameters for the function E, keeping (x_0, z_0) fixed. In practice for each spatial point (x_0, z_0) we perform a non-linear optimization of E over the remaining parameters $\left(v^b, \theta^b, \gamma^b\right)$. This minor optimization problem is significantly less difficult to solve, compared with the original one. In this paper we solve this problem using the Nelder and Mead "Downhill Simplex" algorithm ([14]).

The solution of the global optimization problem has been then reduced to a simpler optimization problem of E^{out} over the space (x_0, z_0). For solving this problem we used the nested grid approach explained in Appendix B. The range of explored model parameters is shown in Tab. 12. The final results for this model (both in windless and wind condition) are shown in Tab. 12 (2A and 2B) and the traveltimes in Fig. 12. The error function is, in both cases, significantly higher than the point source solution (Tab. 12 1B). Furthermore the supposed jet path and altitude is incompatible with observed acoustic phenomena, since it crosses densely urbanized areas where any "boom", neither other phenomena, have been reported.

7 A supersonic sea-air missile?

We also tested the hypothesis that a missile was launched from the sea (or land) during a possible military operation, terminating its path in the atmosphere with an explosion. In this case the model parameters (Tab. 12) are 6 $(x_0, y_0, z_0, v, \theta, \gamma)$, where (x_0, y_0, z_0) are the coordinates of the final blasting point, while the other paramers have the same meaning of the previous case. Also for this problem we perform a splitting of the whole inverse problem, enclosing the optimization over the parameters (v, θ, γ) inside a misfit function:

$$E^{out}(x_0, y_0, z_0) = E\left(x_0, y_0, z_0, v^b, \theta^b, \gamma^b\right), \tag{10}$$

and solving with the hybrid nested grid/downhill simplex (NG/DS) approach. The final result (Tab. 12, 5A and 5B) shows a final blasting point N of Campi Flegrei and a trajectory crossing Ischia (Fig. 13). The final misfit for the model 5B, seems to be a little bit lower than the point source model 1B (Tab. 12). The misfit reduction is balanced by the increase in model complexity (3 vs 6 parameters) and in section 10 we will show that the Akaike Information Criterion suggests that the best choice is model 1B. Anyway also this model does not fit well with the observed acoustic phenomena.

8 A simple bolide model

We suppose then that the recorded signal is the expression of a shock wave generated by a bolide. This hypotesis is supported by cases reported in recent papers ([10], [12]). Following the previous authors we assume a linear trajectory

with constant velocity for the bolide path. The model parameters in this case are $\mathbf{m} = (x_0, y_0, v, \theta, \gamma)$, where x_0 and y_0 are the coordinates of the intersection between the trajectory and the ground, while v is the bolide velocity, θ is the trajectory azimuth and γ is its inclination. For this problem, we define, again, an "outer" misfit function:

$$E^{out}(x_0, y_0) = E\left(x_0, y_0, v^b, \theta^b, \gamma^b\right), \tag{11}$$

and optimize using the hybrid NG/DS approach.

The explored range for each parameter is in Tab. 12, while results are shown in Tab. 12 (3A and 3B) and in Fig. 14. This result has a final misfit (Tab. 12) lower than the point source model (i.e. an atmospheric explosion). Furthermore the point source model itself is not able to explain the "N-wave" signature on seismograms observed in Campi Flegrei. Then we conclude that a bolide is a good explanation for both observed traveltimes and acoustic effects. However a careful observation of waveforms at stations FO9 and OC9 (Fig. 4) shows a shape that does not fit into the "N-wave" model shown in Fig. 6. Then we hypothize that with the hypersonic shock wave we also recorded signals coming from the terminal bolide airblast.

9 Model of a bolide with terminal airblast

In Fig. 15 we give an alternative explanation to the waveforms observed at Ischia, in particular for the station FO9 (Fig.4). We suppose a single, positive, box shaped pressure pulse. The ground velocity generated by this kind of signal differs substantially from the "N-wave" model. While the latter waveform is dominated by two downward directed pulses, in the former the dominant feature are two opposite pulses, the first downward and the second upward (Fig.15C). The response of a short period sensor (Fig.15E) fits well with the observed waveform at FO9. For this reason we suppose that the observed signal at Ischia differs from the rest of the network, being generate by the final bolide airblast rather than the hypersonic shock wave.

We tried then to justify traveltimes with the model of a bolide entering in the atmosphere at a constant velocity v, with azimuth γ and inclination θ. The trajectory stops at the blasting point (x_0, y_0, z_0). An example of wavefronts generated by this kind of trajectory is shown in Fig. 20B.

Also in this case we perform a non-linear optimization using the hybrid NG/DS approach. The explored range of parameters is in Tab. 12. Results in the windless and wind cases are shown in Tab. 12 (4A and 4B) and the final misfit in Tab. 12. Traveltimes for this model are in Fig. 16. The uncertainty on the blasting point location is less than $500\,m$, while the uncertainty estimation on the remaining parameters is discussed in section 11.

This seems clearly the best model that justifies traveltimes, waveforms and acoustic effects. An interesting observation is that, on the basis of traveltime modeling, all the stations of Ischia (FO9, OC9 and CAI) are reached first by the airblast signal, while in the rest of the network the first recorded signal is the "N-wave", followed by the airblast. At all these stations the traveltime difference between the "N-wave" and the airblast should be less than $1\,s$. For this reason it is very difficult detect this second phase on the waveforms, since it appears inside the strong ground oscillations following the "N wave" arrival.

10 Choosing the most realistic model

With and without considering the wind effect, we have examined 10 models. On the basis of traveltime fit (Tab. 12) we deduce that the wind effect is significant for all the considered models, then we restrict our choice over 5 models (1B, 2B, 3B, 4B and 5B).

Among the 3C stations OC9, DMP, STH and BKE, show a clear horizontal polarization of the first arrival (Fig. 17). Unfortunately the particle motion pattern seems to fit well enough for all the proposed models, so we did not used it as a criterion for selecting the best one.

A similar problem has been faced by [25], which used the χ^2 criterion to choose between a model with only a bolide shock wave and another with only a terminal blast. Here we apply the Akaike Information Criterion (AIC) ([1]) for performing the choice.

Each model has a different final misfit, but also a different number of parameters. Using the "Occam's razor" principle, it is intuitive to choose the model having the smallest number of parameters and able to justify observed data. A quantification of this claim is given by the AIC, that is:

$$AIC = -2\ln(likelihood) + 2N_p, \tag{12}$$

where N_p is the number of parameters of the model. Since our dataset is small, compared with the number of parameters, it is better to use a modification of the AIC, defined as ([5]):

$$AICc = -2\ln(likelihood) + 2N_p\frac{N_d}{N_d - N_p - 1}, \tag{13}$$

where N_d is the number of data. Substituting in the previous expression, the likelihood function defined in eq.3 we obtain:

$$AICc = 2E + 2N_p\frac{N_d}{N_d - N_p - 1}. \tag{14}$$

The $AICc$ is minimum for the model that best satisfies the Occam's principle. In Tab. 12 all the models misfits and AICc is shown. On the basis of this reasoning we deduce that the model 4B is the best.

11 Precise bolide trajectory determination

We investigate now about the uncertainties of the parameters γ, θ and v for the model 4B.

In Fig. 18 we represent the misfit as function of θ and γ keeping fixed the other parameters (see Tab. 12). The shape of this function gives a clear idea about the non-linearity beyond this kind of inverse problems. The main features of this function are an "high misfit" region (in red), a "flat" region (in cyan) and a single absolute minimum (in magenta). The red region spans all the model having a trajectory incompatible with observed data. The flat region is composed by all the trajectories making all the stations reached only by the airblast waves. In this case obviously varying the inclination and the azimuth has no effect on the misfit. From the small area of the minimum region, that

marks the only allowed combinations of θ and γ that justifies observed traveltimes, we conclude then that the trajectory parameters shown in Tab. 12 are well determined, with an uncertainty of few degrees.

Fig. 19 represents the misfit function versus the bolide velocity. It shows an almost flat region beyond about $30\,km/s$. This is because for very high Mach numbers, the Mach cone is so sharp, that wavefronts becomes almost cylindrical. Then for very high bolide speeds, a further velocity increment has a negligible effect on traveltimes. The best fit model reported in Tab. 12 gives a best fit velocity of about $60\,km/s$. Anyway, on the basis of Fig. 19 we claim, from our observations, that only a lower boundary to the bolide velocity, at about $30\,km/s$, may be established.

12 Conclusions

In conclusion, we presented a case of seismic detection of a bolide airblast without direct visual witness. Basing our analysis on advanced forward modeling, inversion techniques and on a robust statistical inference, we have shown that this hypothesis is strongly supported by observed traveltimes, waveforms and acoustic effects.

We have shown how methods, commonly used in seismological practice for traveltime computation and earthquake location in heterogeneous media, may be successfully applied to model infrasonic propagation with only slight adaption.

We have also demonstrated that the wind effect on traveltime modeling and then on source location is not negligible. Discarding wind effect may lead to an overestimate of the height of the blasting point and conseguently to underestimates of the bolide energy.

The non-linear inverse method, used for determining simultaneously the blasting point position, the trajectory and the bolide velocity, have shown to be efficient, ensuring a robust determination of parameters also for complex misfit functions as Fig. 18.

Statistical inferences, with the aid of AICc, gives a clear indication that the best model is the bolide with final airblast. The blasting point has been determined with an high accuracy (less than $500\,m$) at an height of about $11.5\,km$. The trajectory has an azimuth of 220^o and an inclination of 56^o. The lower limit for the entrance velocity is about $30\,km/s$.

This model predicts that first-arrivals at Ischia comes from the blasting point, while at the rest of the network they comes from the Mach cone. This observation is confirmed by waveforms that shows in Campi Flegrei area a clear "N-wave" pattern, while in Ischia island a single positive pressure pulse best justifies seismic recordings.

It is also interesting to notice that the acoustic wave amplitude related to a quasi-spherical wavefront decays as d^{-1} (where d is the distance), while for a quasi-cylindrical wavefront decays as $d^{-1/2}$. This may justify why perceptible acoustic effects have been reported from Ischia, but not far away.

A further step in the analysis of this phenomenon may be given by ground motion amplitude modeling and inversion. In our case this is a hard task, because the soil structure strongly varies from one site to another, due to the complex volcanological setting of the Neapolitan area.

Appendix A - Fast traveltime computation for standing and moving sources in a realistic atmospheric model

During the last 20 year, in seismological scientific literature, many algorithms for the fast computation of first arrival travel times in complex propagation media appeared ([13]). Among those, the class of algorithms based on the finite-difference solution of the eikonal equation (FDE) is one of the most fast and efficient from a computational point of view ([26]).

In this paper we use the Podvin and Lecomte ([16]) algorithm (PL) for modeling traveltimes in a realistic heterogeneous atmospheric model. Since we use only 1D models, traveltimes posses a radial simmetry respect a point source, then only a 2D (distance-height) computation is needed. The PL algorithm computes traveltimes over a regular grid. In all the computations we used a $250\,m$ spacing. Traveltimes over a finer grid may be obtained by simple bilinear interpolation ([17]). An example of computation for a point source is shown in Fig. 20.

For computing traveltimes related to an arbitrary moving supersonic object we use the following strategy, based on the Fermat principle. We parametrize the trajectory as:

$$\mathbf{s} = \mathbf{s}(t), \tag{15}$$

where $\mathbf{s}$ is the path of the object a t is the time. Then, for a given receiver $\mathbf{x}_R$, the traveltime related to each point of the path is:

$$T = T\left(\mathbf{s}\left(t\right)\right) = T\left(t\right). \tag{16}$$

This value may be computed using the previous mentioned PL algorithm. Our task is now to find the value t that make the traveltime minimum for our observing point. This may be achieved just using common 1D non-linear optimization algorithms. In this paper we use the golden search algorithm ([17]) that have shown to be fast and robust enough for our purposes.

A dramatic optimization in computation times is achieved using the reciprocity theorem for first arrival traveltimes. Instead of computing arrival times from each point of the trajectory to each receiver, we do the converse. So the number on PL algorithm runs is reduced to just the number of receivers. For this reason a traveltime grid for each $\mathbf{x}_R$ may be computed once and stored in the RAM.

On a typical modern computer (Intel®Pentium IV®, 3.0 GHz, 512 KB cache, 512 MB RAM), a single run of PL algorithm on a 1500x400 grid requires about $0.066\,s$, and the computation of traveltime for a point source at 20 receivers requires about $2 \cdot 10^{-3}\,s$, while for a linear trajectory requires about $2.2 \cdot 10^{-2}\,s$. This means that each second about 450 models can be explored.

Appendix B - A nested grid approach for non-linear optimization

The problem of finding a best fit solution for a linear trajectory (airplane , missile and fireball paths) is a not a simple task. The strong non-linearity of the

misfit fuction (as in Fig. 18) makes the optimization task non trivial ([21]) and different optimization methods have been proposed in geophysics as Simulated Annealing and Genetic Algorithms ([20]) for solving this kind of problems. We perform non-linear optimization using a massive search in the model space. A simple grid search approach over the whole range of parameters would lead to cumbersome computation times. We propose an approach based on a multiple search over progressively finer grids.

The first grid spans the range $\left[a_1^0, b_1^0\right] \times \ldots \times \left[a_N^0, b_N^0\right]$, where a_i^0 and b_i^0 are the minimum and maximum admissible values for the parameter i. After a rough preliminary grid search over this range, a best fit model $\mathbf{m}^0$ is found. The next search is performed over the range $\left[m_1^0 - \frac{l_1^0}{k}, m_1^0 + \frac{l_1^0}{k}\right] \times \ldots \times \left[m_N^0 - \frac{l_N^0}{k}, m_N^0 + \frac{l_N^0}{k}\right]$, where $l_i^0 = b_i^0 - a_i^0$ and k is a shrinking constant. In this paper we use $k = 1.5$. So at each iteration the size of the grid is reduced and the search is restricted around the best fit model found in the previous iteration. The process is repeated until the size of the grid shinks below a given threshold.

References

[1] H. Akaike. A new look at the statistical model identification. *IEEE Trans. Autom. Control.*, AC-9:716–723, 1974.

[2] Anonymous. Noaa-cires cdc ncep/ncar reanalysis 1 database. http://www.cdc.noaa.gov/cdc/data.ncep.reanalysis.html.

[3] Anonymous. U.s. standard atmosphere. Technical report, U.S. Government Printing Office, Washington D.C., 1976.

[4] P.G. Brown, R.D. Whitaker, and D.O. ReVelle. Multi-station infrasonic observations of two large bolides: Signal interpretation and implication for monitoring of atmospheric explosions. *Geoph. Res. Lett.*, 29(13), 2002.

[5] K.P. Burnham and D.R. Anderson. *Model selection and multimodel inference: a practical-theoretic approach.* Springer, 2002.

[6] L.G. Evers and H.W. Haak. Listening to sounds from an exploding meteor and oceanic waves. *Geoph. Res. Lett.*, 28(1):41–44, 2001.

[7] L. Foschini. On the atmospheric fragmentation of small asteroids. *Astronomy and Astrophysics*, 365:612–621, 2001.

[8] M.A. Garcés, R.A. Hansen, and K.G. Lindquist. Traveltimes for infrasonic waves propagating in a stratified atmosphere. *Geoph. J. Int.*, 135:255–263, 1998.

[9] Y. Ishihara, M. Furumoto, S. Sakai, and S. Tsukada. The 2003 kanto large bolide's trajectory determined from shockwaves recorded by a seismic network and images taken by a video camera. *Geoph. Res. Lett.*, 13, 2004.

[10] Y. Ishihara, S. Tsukada, S. Sakai, Y. Hiramatsu, and M. Furumoto. The 1998 miyako fireball's trajectory determined from shock wave records of a dense seismic array. *Earth Planets Space*, 55:e9–e12, 2003.

[11] H. Kanamori, J. Mori, D.L. Anderson, and T.H. Heaton. Seismic excitation by the space shuttle columbia. *Nature*, 349:781–782, 1991.

[12] C.A. Langston. Seismic ground motion from a bolide shock wave. *J. Geoph. Res.*, 109(B1), 2004.

[13] A. Leidenfrost, N. Ettrich, D. Gajewski, and D. Kosloff. Comparison of six different methods for calculating traveltimes. *Geoph. Prosp.*, 47:269–297, 1999.

[14] J.A. Nelder and R. Mead. A simplex method for function optimization. *comp. J.*, 7:308–313, 1965.

[15] O.R. Norton. *The Cambridge Encyclopedia of Meteorites.* Cambridge University Press, 2002.

[16] P. Podvin and I. Lecomte. Finite difference computation of traveltimes in very contrasted velocity models: A massively parallel approach and its associated tools. *Geoph. J. Int.*, 195:271–284, 1991.

[17] W.H. Press, S.A. Teukolsky, W.T. Vetterling, and B.P. Flannery. *Numerical Recipes in C++.* Cambride University Press, 2002.

[18] J. Pujol, P. Rydelek, and T. Bohlen. Determination of the trajectory of a fireball using seismic network data. *Bull. Seism. Soc. Amer.*, 95(4):1495–1509, 2005.

[19] D.O. ReVelle. On meteor-generated infrasounds. *J. Geoph. Res.*, 81:1217–1240, 1976.

[20] M. Sen and P.L. Stoffa. *Global optimization methods in Geophysical Inversion.* Elsevier, Amsterdam., 1995.

[21] R. Snieder. The role of nonlinearity in inverse problems. *Inverse Problems*, 14:387–404, 1998.

[22] B. Sturtevant, J.E. Cates, and H. Kanamori. Studies of sonic booms with seismic networks. *J. Acoust. Soc. Amer.*, 97(5), 1995.

[23] A. Tarantola. *Inverse Problem Theory and Methods for Model Parameter Estimation.* Society for Industrial and Applied Mathematic, 2004.

[24] J.B. Tatum. Fireballs: Interpretation of airblast data. *Meteoritics and Planetary Science*, 34:571–585, 1999.

[25] J.B. Tatum. Sound from a fireball - distinguishing between the hypersonic shock front and the terminal burst. *Planetary and Space Science*, 48:921–923, 2000.

[26] J. Vidale. Finite-difference calculation of travel times. *Bull. Seism. Soc. Amer.*, 78(6):2062–2076, 1988.

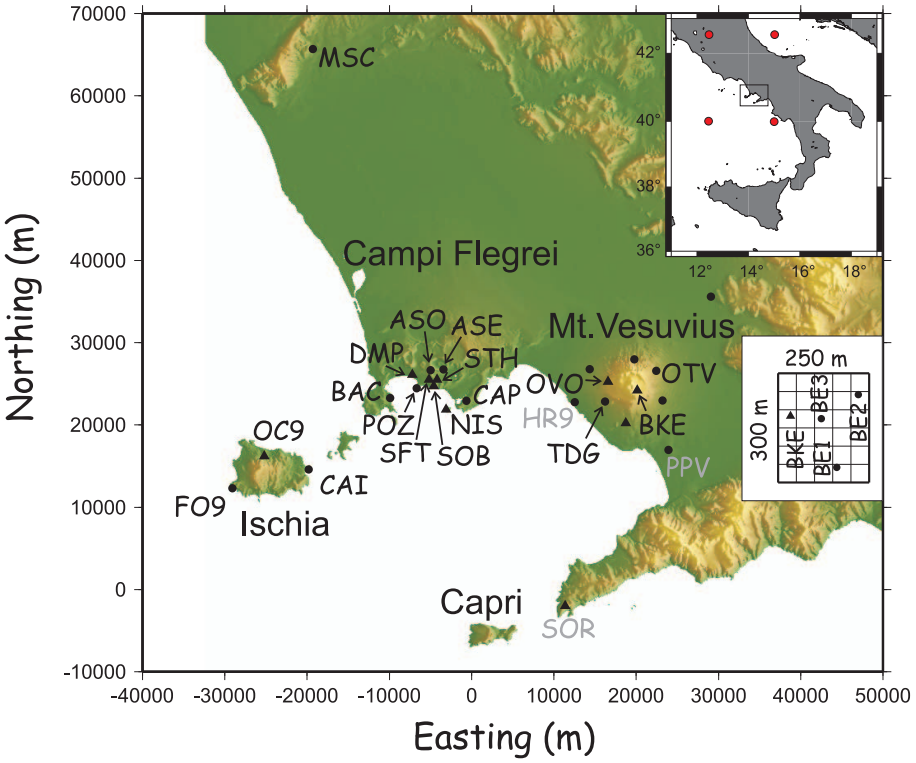

Figure 1: Map of the Gulf of Naples and the surrounding region, with seismic stations (circles, 1C and triangles 3C). Stations with gray name or no name have not recorded any significant signal and are not used in the analyses. All listed stations but SOB are equipped with short period sensors. Three more stations composing a small seismic array close ($< 200m$) to BKE (BE1, BE2 and BE3) are shown in the inset on the right. The red points in the small map of Italy (upper right) are the points where atmospheric data from NOAA-CIRES CDC (NCEP/NCAR Reanalysis 1) are available. The coordinates are the cartesian reference system of our analysis.

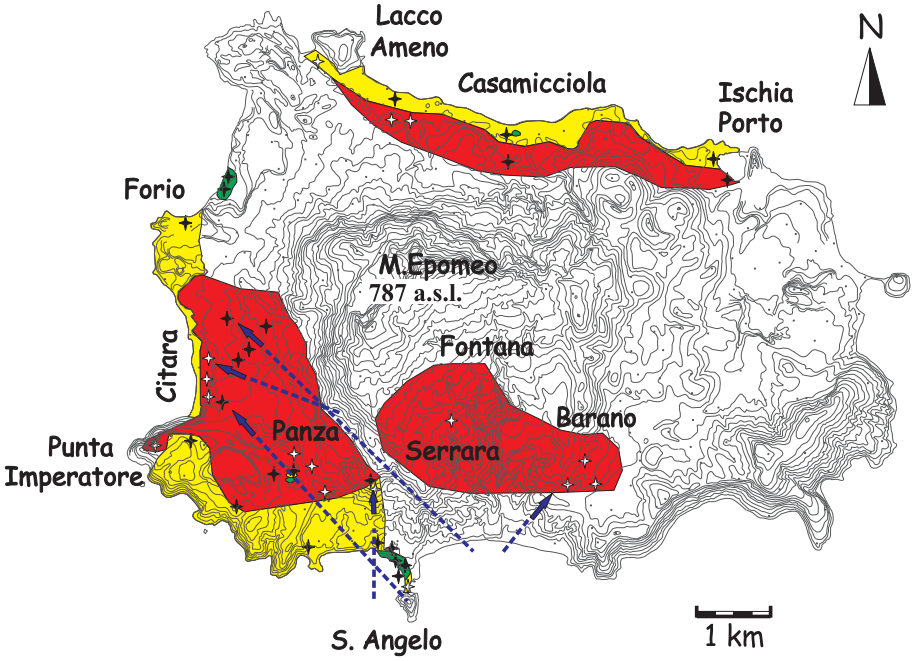

Figure 2: Observed acoustic phenomena, based on witness report. Red areas indicates the maximum level of sound intensity, while yellow areas represents a lower one (see text for details). Green spots represents minor areas where the sound has been barely or not heard. Areas where no informations have been collected are painted white. Interview points are represented by stars. Black stars indicates sites where informations comes directly from the interviewed person, while white stars represent sites where informations have been gathered indirectly (i.e. a person reporting notice from another one). Blue arrows indicates the perceived direction of the origin of the sound. Dashed lines join the interview point and the supposed sound source speculated by interviewed people.

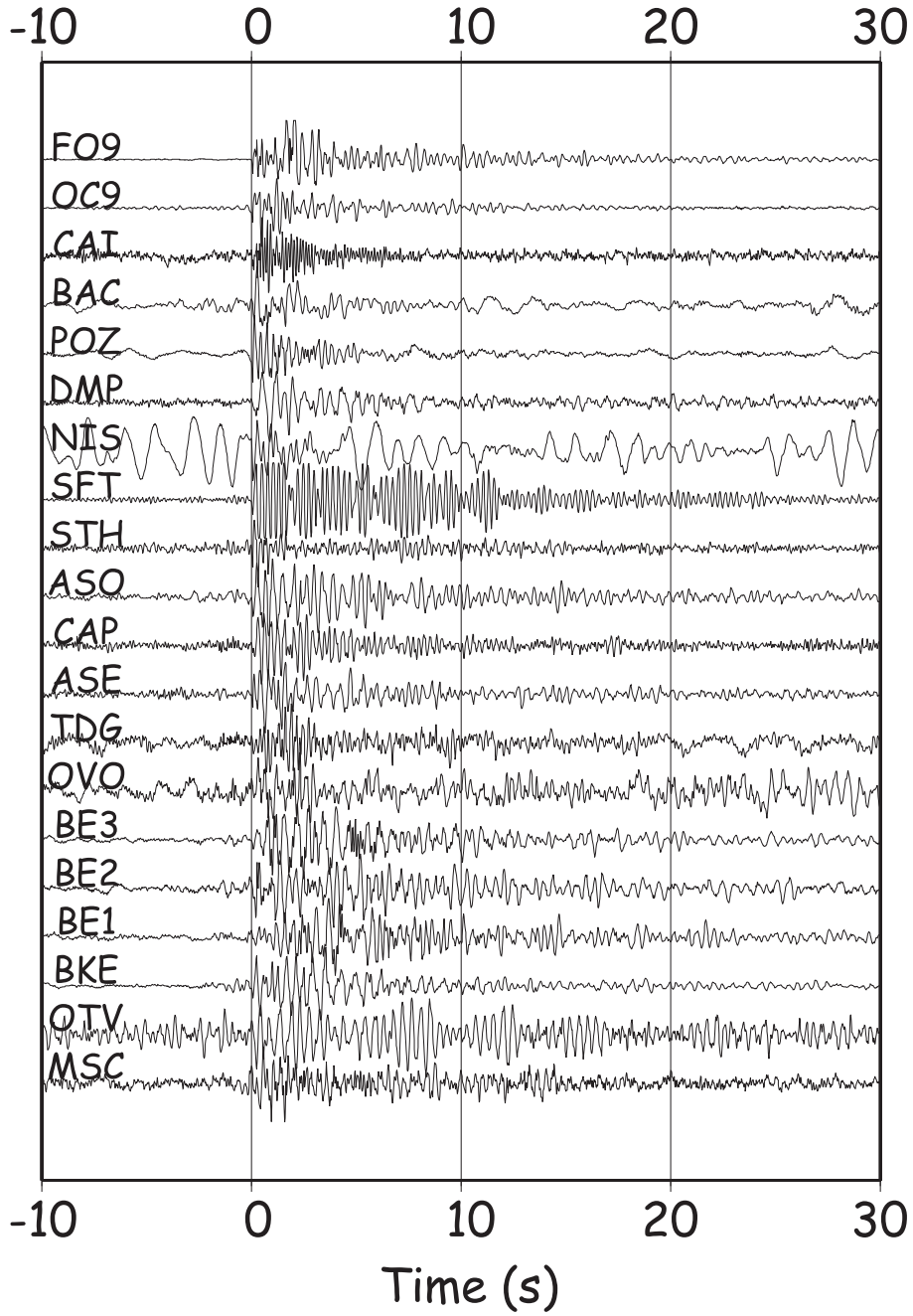

Figure 3: Velocity waveforms recorded by the INGV-OV seismic network. Traces are normalized and aligned on the supposed first acoustic arrival.

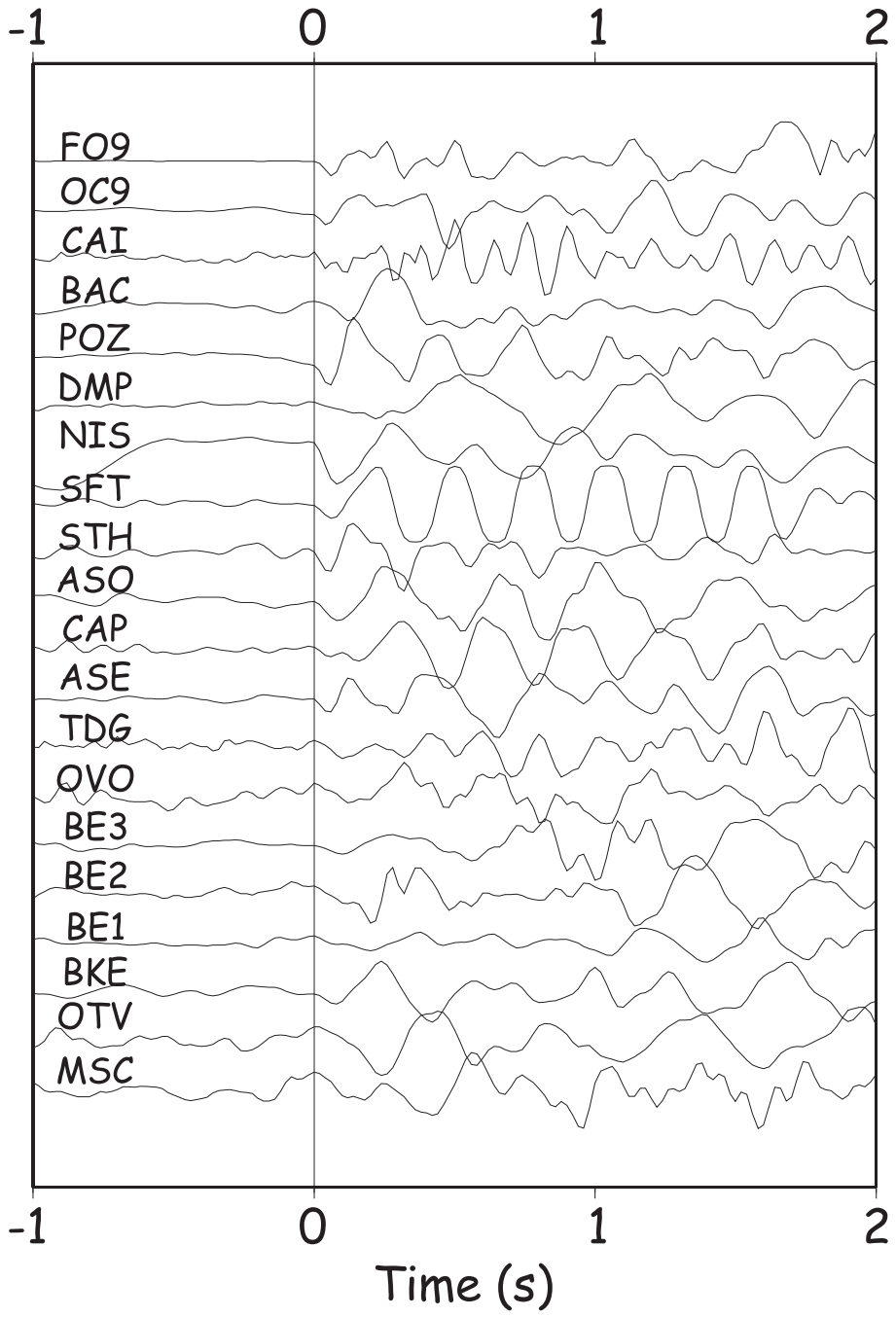

Figure 4: Velocity waveforms recorded by the INGV-OV seismic network. Traces are normalized and aligned on the supposed first acoustic arrival. Note the anomalous waveform of SFT, due to electronic clipping of the signal.

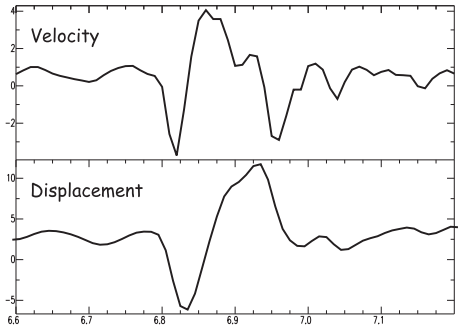

Figure 5: The upper trace shows the velocity seismogram of the vertical component of the broadband station SOB, note the "W" shaped signal. The lower trace shows, the displacement, exhibiting a reverse "N" shape.

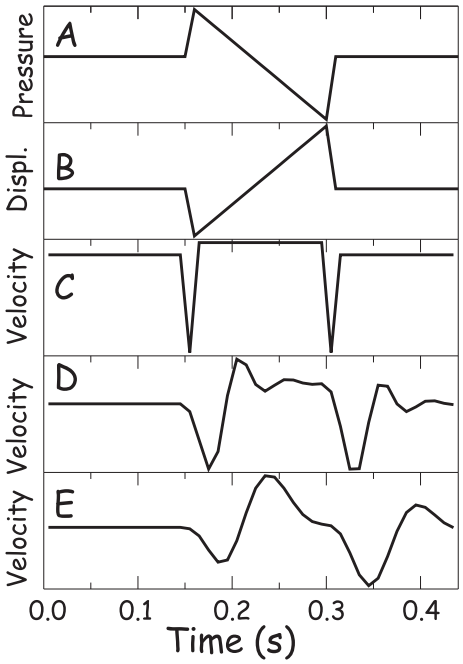

Figure 6: Schematic illustration of the vertical ground movement generated by an "N-wave". In A it is shown the pressure pattern of an "N-wave", while in B the true ground displacement (opposite to the pressure). Its time derivative, the ground velocity, is shown in C. D is the theoretical seismogram recorded by a broadband sensor with flat frequency responde between 0.025 and 25 Hz. The same is in E for a short period sensor, with flat response between 1 and 12 Hz. Note that the "W" shape of the velocity seismogram may be hard to recognize on a short period recording.

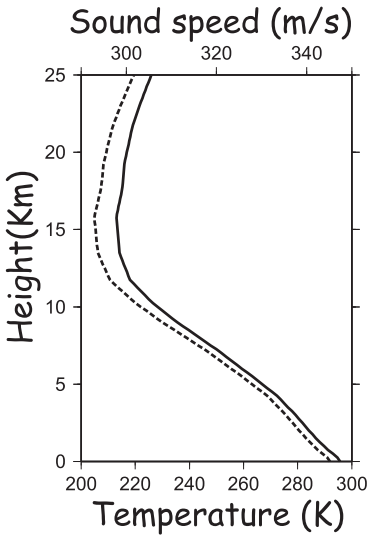

Figure 7: Average value of air temperature up to 25 Km (continuous line) and the matching sound speed (dotted line). Data are from NOAA-CIRES CDC (NCEP/NCAR Reanalysis 1). Values are interpolated over the nearest 4 spatial points (see Fig. 1) and the 2 nearest times (12:00 and 18:00 GMT).

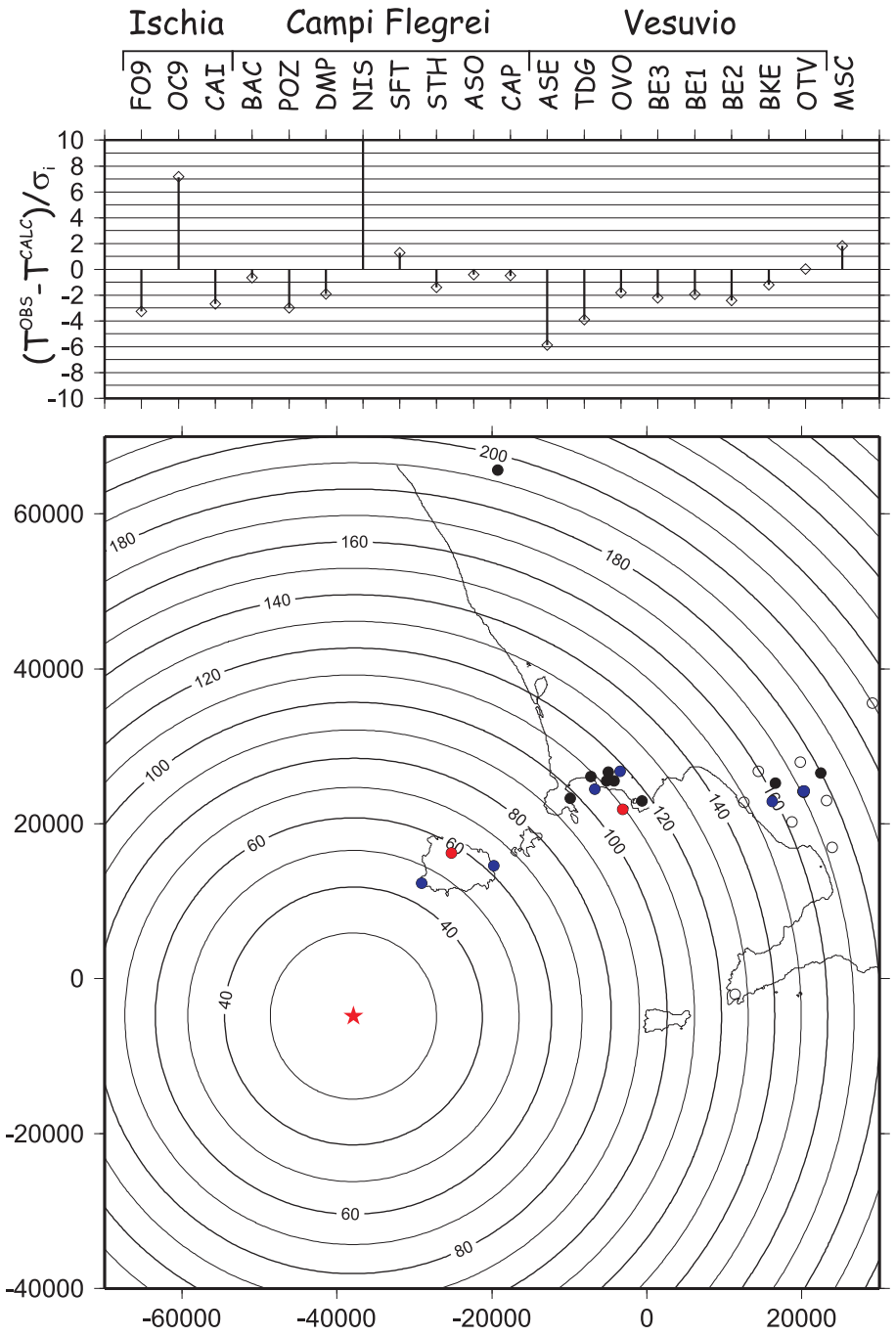

Figure 8: Theoretical traveltimes at $z = 0$ for the best fit point source solution (1A in Tab. 12) (isolines in s). On the top, relative residuals (i.e. $\left(t^i_{obs} - t^i_{calc}\right)/\sigma_i$) for each station are shown. The red star on the map is the position of the source. Small circles indicates station positions. Red circles represents stations having a relative residual larger than 2, while blue ones have a residual lower than -2. Empty circles marks position of stations which have not recorded a significant signal.

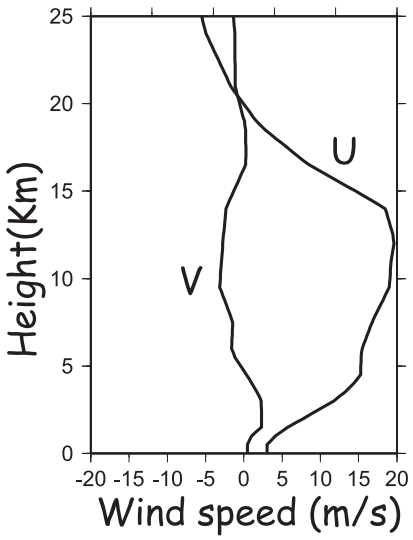

Figure 9: Wind speed model for the range 0-25 Km. Note the prevailing wind along the U (Est) direction.

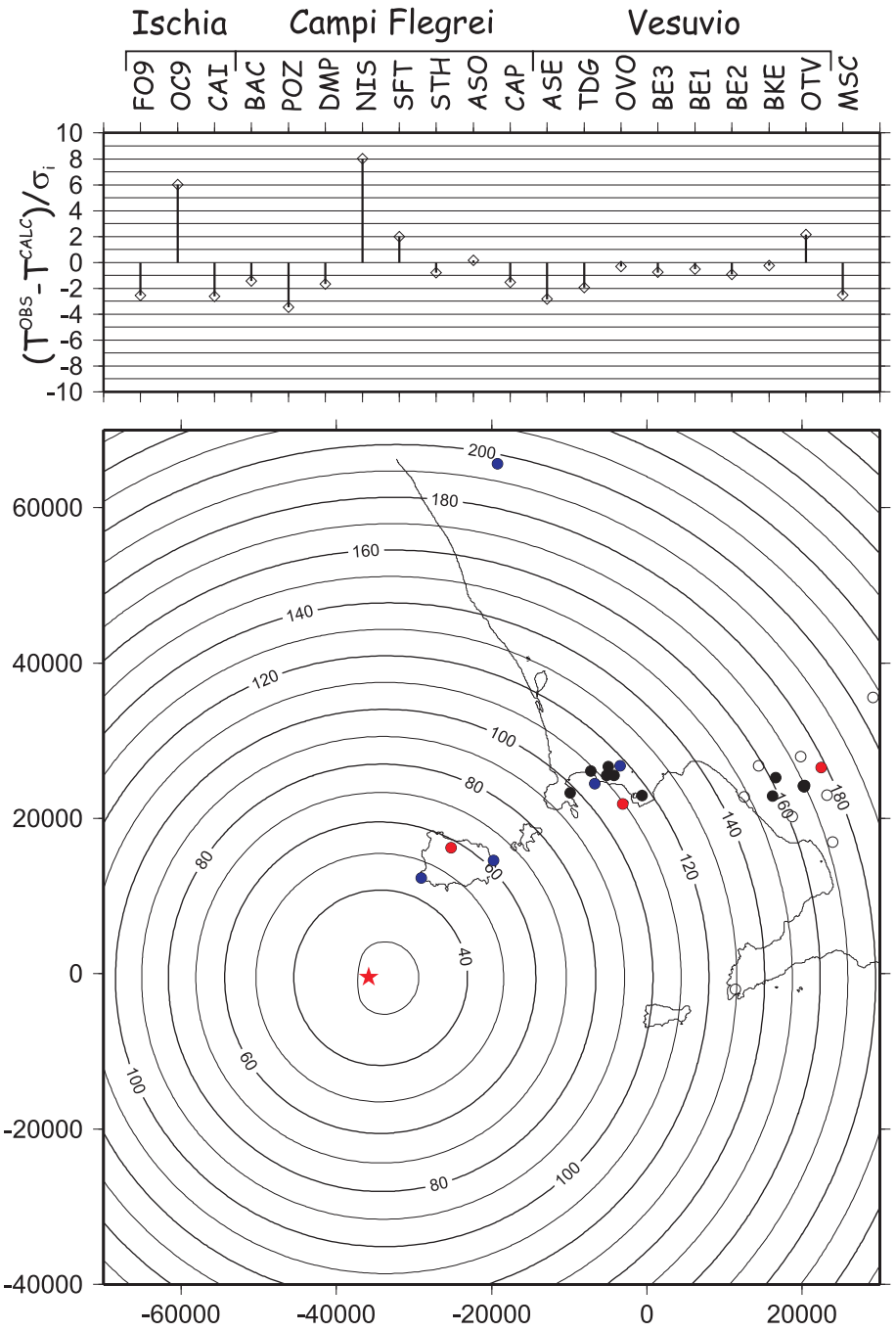

Figure 10: Theoretical traveltimes for the best fit point source solution (1B in Tab. 12) including wind effect. See caption of Fig. 8 for details about the meaning of symbols.

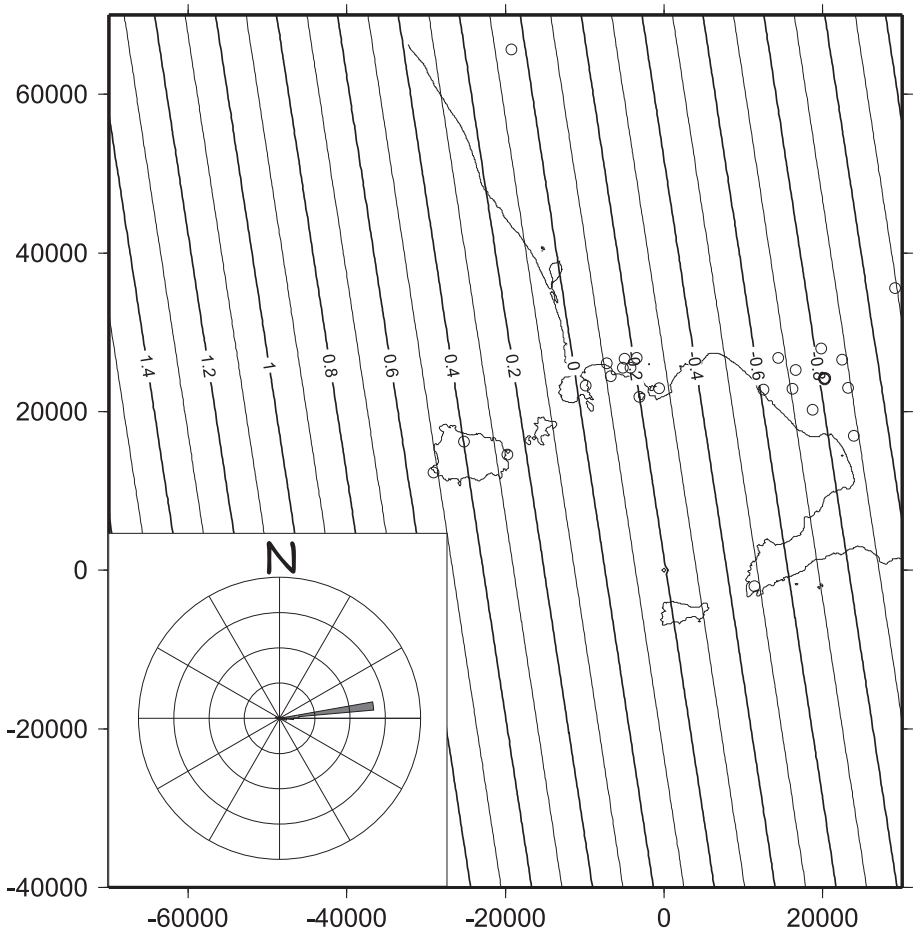

Figure 11: Traveltime differences between the wind and the windless theoretical modeling, using the model 1B (see Tab. 12). The lower left inset represents a rose diagram for the wind directions. Note the good coincidence between the prevailing wind direction ($N83^o$) and the normal to traveltime difference isolines.

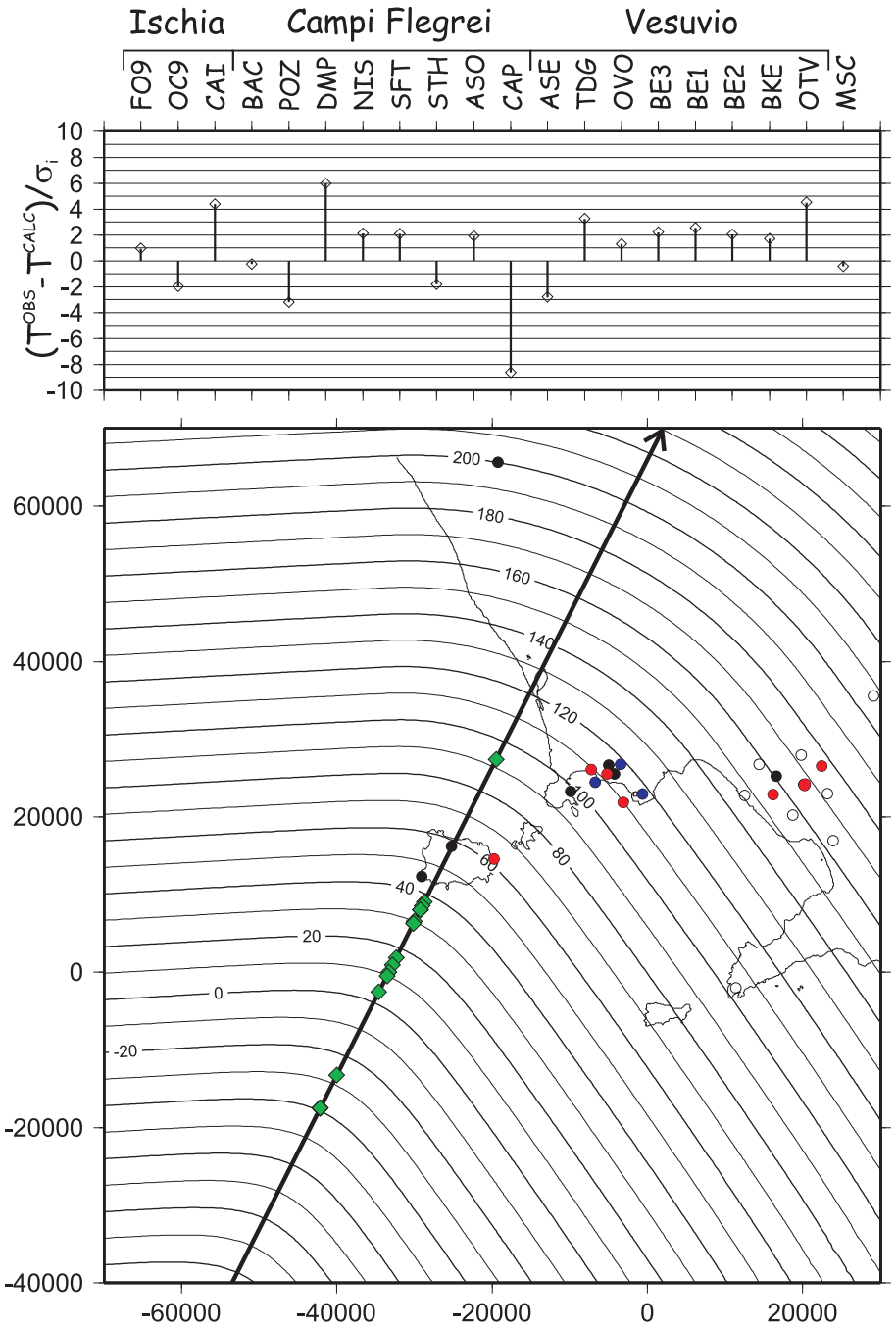

Figure 12: Theoretical traveltimes for the best fit supersonic jet model (2B in Tab. 12) including wind effect. The solid line is the trajectory. Green diamonds on the trajectory are the source points related to each station. See caption of Fig. 8 for details about the meaning of other symbols.

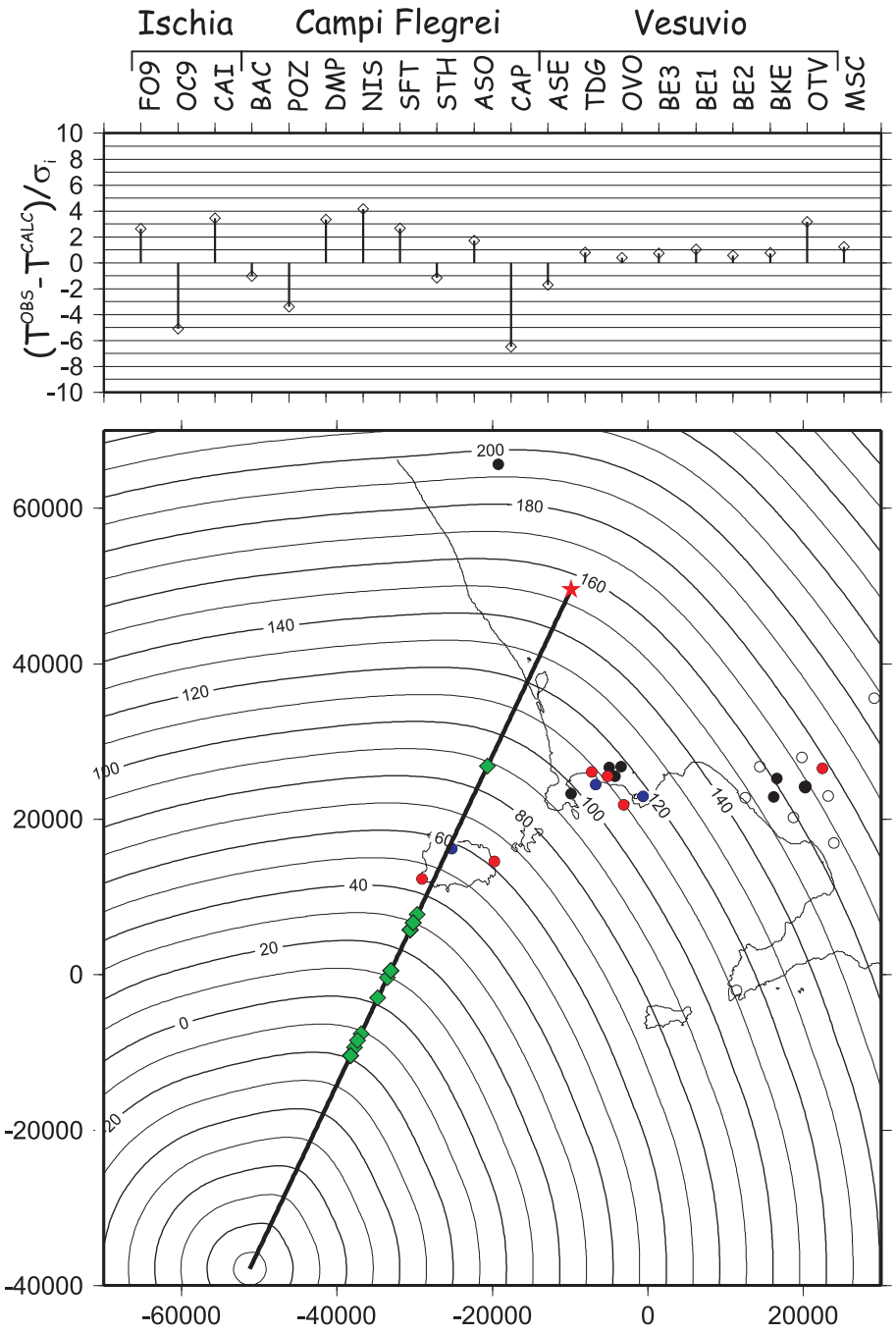

Figure 13: Theoretical traveltimes for the best fit sea-air missile model (5B in Tab. 12). See Fig. 8 and Fig. 12 for details about the meaning of other symbols.

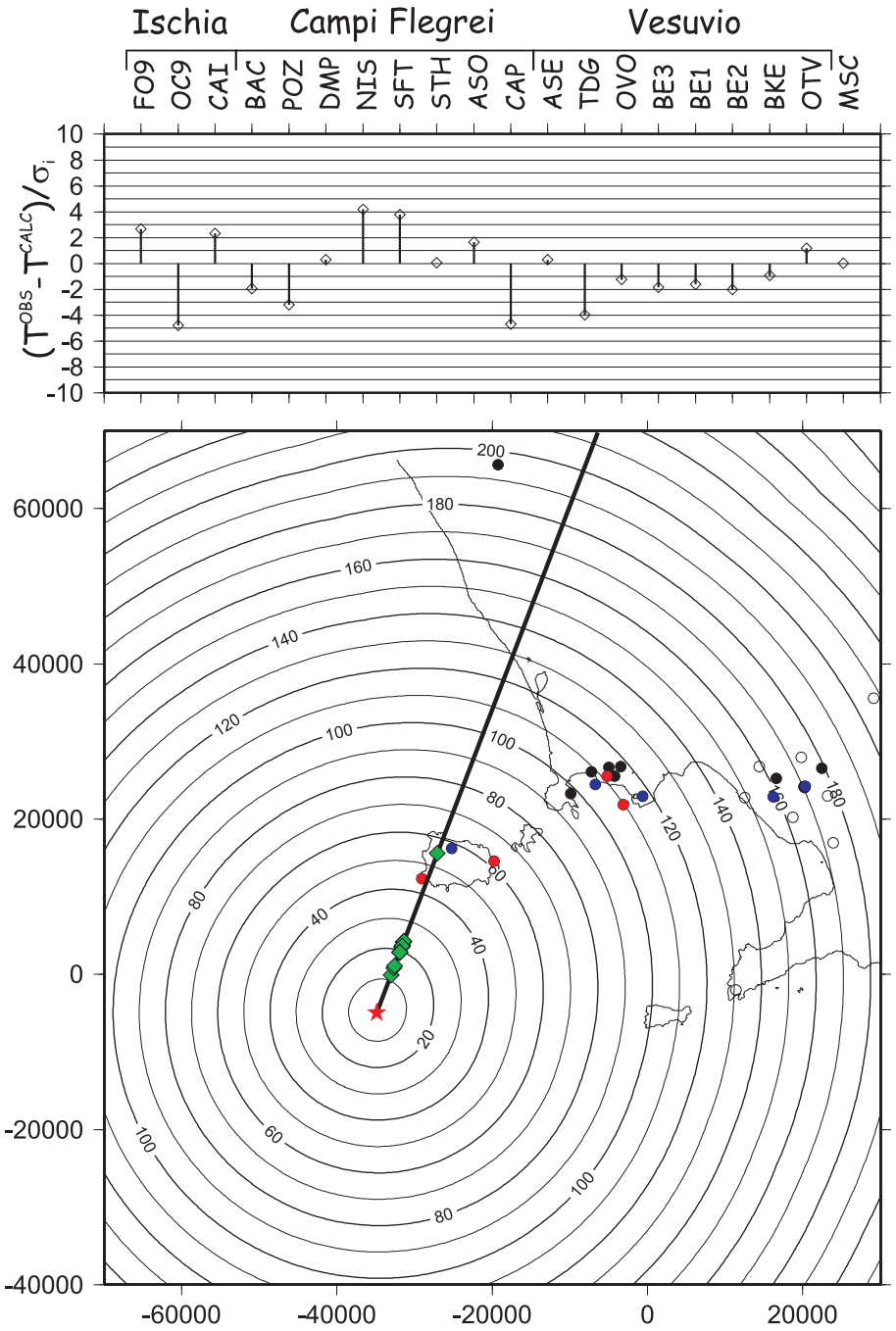

Figure 14: Theoretical traveltimes for the best fit bolide model (3B in Tab. 12). See Fig. 8 and Fig. 12 for details about the other symbols.

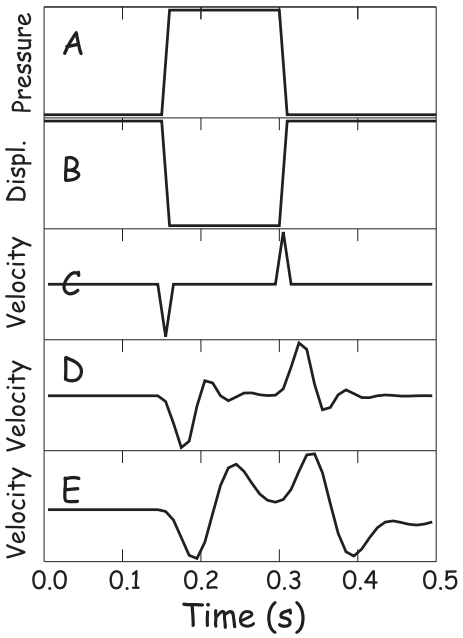

Figure 15: Schematic illustration of the vertical ground movement generated by an explosion. In A the pressure pattern, with a single, sharp, pressure pulse is shown. The ground displacement is shown in B and the ground velocity in C. Note the difference between the velocity in C and the ground velocity for a "N-wave" in Fig. 6. In D the theoretical seismogram recorded by a broadband sensor with flat frequency response between 0.025 and 25 Hz is shown. The same is for a short period sensor, with flat response between 1 and 12 Hz is shown in E.

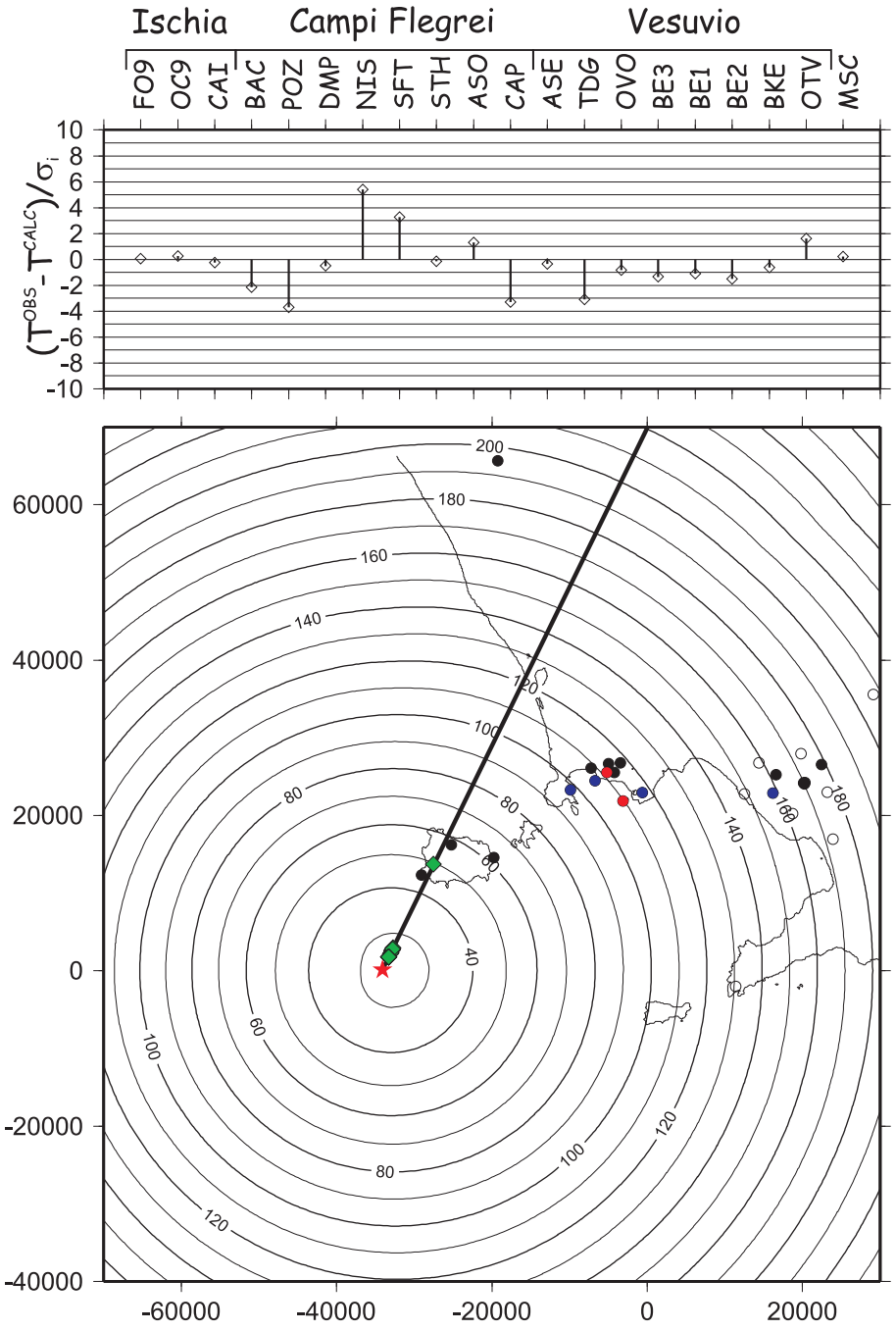

Figure 16: Theoretical traveltimes for the best fit model of bolide with airblast (4B in Tab. 12) including wind effect. See Fig. 8 and Fig. 12 for details about the other symbols. The greed diamonds are relative only to Campi Flegrei, Vesuvius and MSC stations, since the wavefronts over Ischia, comes directly from the blasting point.

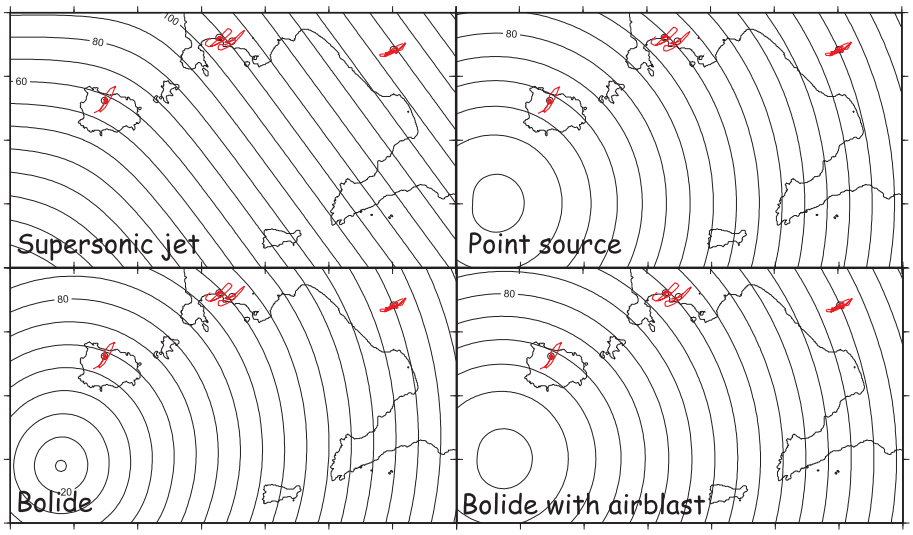

Figure 17: Comparison between particle motion at 3C stations showing a good polarization (OC9, DMP, STH, BKE) plotted on theretical traveltimes for models 2B (upper left), 1B (upper right), 3B (lower left) and 4B (lower right).

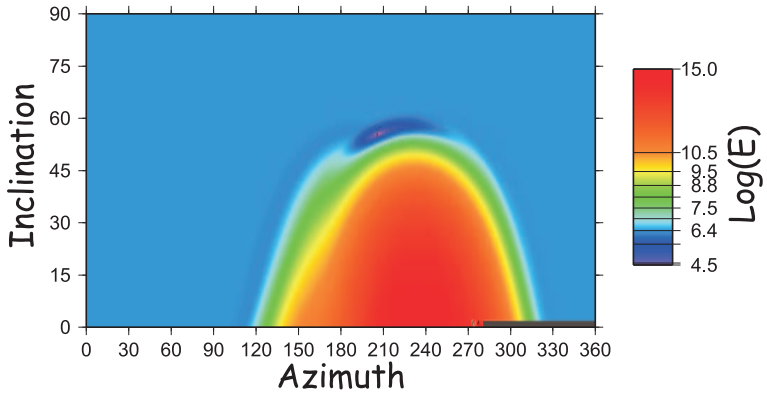

Figure 18: Logarithm of the misfit as function of azimuth (γ) and inclination (θ), keeping fixed all the other parameters for the model 4B of Tab. 12). Note the wide flat region corresponding to a value of $log(E) = 6.391$.

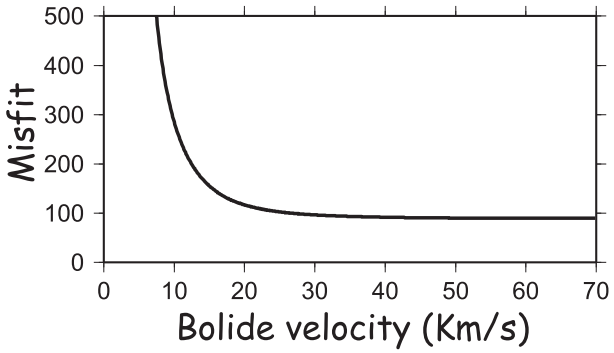

Figure 19: Misfit as a function of bolide velocity. Note that for values beyond $30\,km/s$ the function is almost flat.

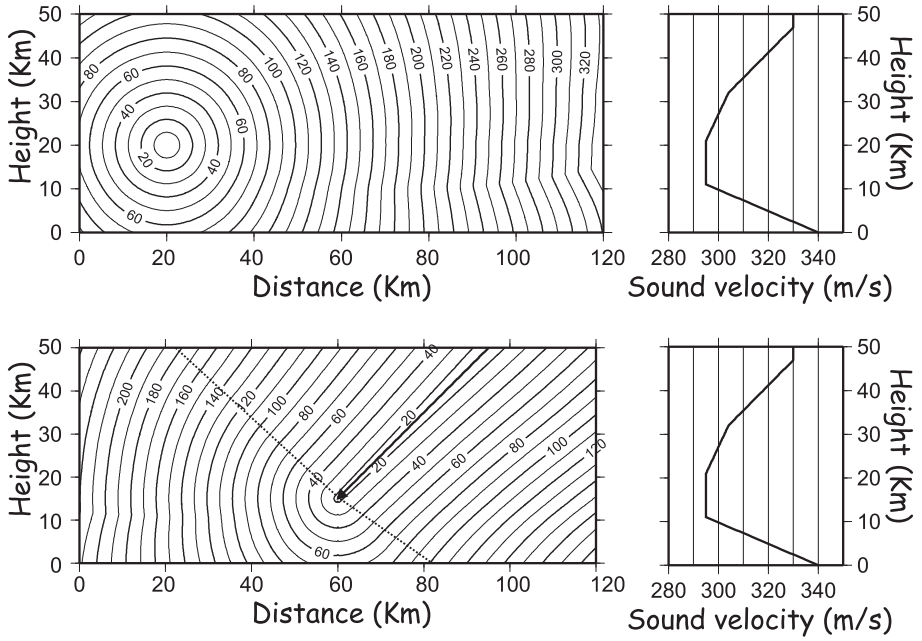

Figure 20: The top picture shows traveltimes from a point source at $x = 20\,Km$ and $z = 20\,Km$. The lower one shows traveltimes for a bolide entering in the atmosphere at a constant speed of $30\,km/s$ and exploding at an height of 15 km. The dotted line marks the separation between the region reached first by the airblast (on the left) and the region reached first by the Mach cone. The sound speed model used for computation is shown on the right.

Station	**Type**	**Time**	**Uncertainty**
FO9	1C	44.72	0.05
OC9	3C	57.61	0.05
CAI	1C	62.15	0.05
BAC	1C	97.56	0.15
POZ	1C	106.31	0.05
DMP	3C	108.50	0.05
NIS	3C	110.03	0.05
SFT	3C	111.70	0.05
STH	3C	113.52	0.1
ASO	1C	114.24	0.12
CAP	1C	116.87	0.05
ASE	1C	117.45	0.05
TDG	1C	157.08	0.4
OVO	3C	161.73	0.7
BE3	1C	169.25	0.8
BE1	1C	169.40	0.8
BE2	1C	169.45	0.8
BKE	3C	169.38	1.2
OTV	1C	180.00	0.8
MSC	1C	195.32	0.5

Table 1: Observed acoustic arrival times relative to starting time 15:10:00.00 GMT. The second column indicates if the station has single (1C) or three components (3C). The fourth column contains uncertainty related to the observed traveltimes.

Description	$\mathbf{x_0}$**(m)**	$\mathbf{y_0}$**(m)**	$\mathbf{z_0}$**(m)**	**v(m/s)**	$\theta(^\circ)$	$\gamma(^\circ)$
Point source	[-70000,30000]	[-40000,20000]	[0,50000]	-	-	-
Jet	[-100000,100000]	-	[0,50000]	[250,2000]	[-20,20]	[0,360]
Bolide	[-70000,30000]	[-40000,20000]	-	[300,70000]	[0,90]	[0,360]
Blast	[-70000,30000]	[-40000,20000]	[0,50000]	[300,70000]	[0,90]	[0,360]
Missile	[-70000,30000]	[-40000,20000]	[0,50000]	[250,2000]	[-90,0]	[0,360]

Table 2: Range of parameters used in the optimization problems. See text for details about the meaning of them.

Model	**Description**	**Wind**	$\mathbf{x_0}$**(m)**	$\mathbf{y_0}$**(m)**	$\mathbf{z_0}$**(m)**	**v(m/s)**	$\theta(^\circ)$	$\gamma(^\circ)$
1A	Point	NO	-37885	-4831	22017	-	-	-
1B	Point	YES	-35875	-418	15173	-	-	-
2A	Jet	NO	-33630	-	19071	359	5.5	27.0
2B	Jet	YES	-33315	-	10528	406	-3.0	26.8
3A	Bolide	NO	-36660	-6368	-	10010	55.2	215.8
3B	Bolide	YES	-34865	-4939	-	10155	56.9	200.3
4A	Blast	NO	-34030	-1413	14180	10101	55.4	219.6
4B	Blast	YES	-34084	125	11574	59990	55.6	205.7
5A	Missile	NO	-14874	35311	19037	399	-2.9	26.8
5B	Missile	YES	-9875	49601	24686	485	-14.1	25.3

Table 3: This table contains a summary of the best-fit parameters for all the considered models. The physical meaning of parameters for each model is different, see text for details.

Model	**Desciption**	**Wind**	**N**	**E**	**AICc**
1A	Point	NO	3	275.5	558.5
1B	Point	YES	3	162.1	331.7
2A	Jet	NO	5	235.4	485.1
2B	Jet	YES	5	219.4	453.1
3A	Bolide	NO	5	242.6	499.5
3B	Bolide	YES	5	135.5	285.3
4A	Blast	NO	6	104.1	226.7
4B	Blast	YES	6	89.8	**198.1**
5A	Missile	NO	6	218.8	456.1
5B	Missile	YES	6	157.4	333.3

Table 4: Number of parameters (N), misfit (E) and Akaike Information Criterion (AICc) for each considered models.